Received: 11 March 2024 | Revised: 20 August 2024 | Accepted: 4 September 2024

DOI: 10.1002/pro.5179

RESEARCH ARTICLE

THE PROTEIN SOCIETY WILEY

Pathological C-terminal phosphomimetic substitutions alter the mechanism of liquid–liquid phase separation of TDP-43 low complexity domain

Raza Haider[1] | **Brandon Shipley**[2] | **Krystyna Surewicz**[1] | **Michael Hinczewski**[2] | **Witold K. Surewicz**[1]

[1]Department of Physiology and Biophysics and the Case Western Reserve University, Cleveland, Ohio, USA

[2]Department of Physics, Case Western Reserve University, Cleveland, Ohio, USA

Correspondence
Michael Hinczewski, Department of Physics, Case Western Reserve University, Cleveland, Ohio, USA.
Email: mxh605@case.edu

Witold K. Surewicz, Department of Physiology and Biophysics and the Case Western Reserve University, Cleveland, Ohio USA.
Email: wks3@case.edu

Funding information
National Institutes of Health, Grant/Award Numbers: RF1 AG061797, F30 AG071339-03, T32 NS077888, T32 GM007250

Review Editor: Jean Baum.

Abstract

C-terminally phosphorylated TAR DNA-binding protein of 43 kDa (TDP-43) marks the proteinaceous inclusions that characterize a number of age-related neurodegenerative diseases, including amyotrophic lateral sclerosis, frontotemporal lobar degeneration and Alzheimer's disease. TDP-43 phosphorylation at S403/S404 and (especially) at S409/S410 is, in fact, accepted as a biomarker of proteinopathy. These residues are located within the low complexity domain (LCD), which also drives the protein's liquid–liquid phase separation (LLPS). The impact of phosphorylation at these LCD sites on phase separation of the protein is a topic of great interest, as these post-translational modifications and LLPS are both implicated in proteinopathies. Here, we employed a combination of experimental and simulation-based approaches to explore this question on a phosphomimetic model of the TDP-43 LCD. Our turbidity and fluorescence microscopy data show that phosphomimetic Ser-to-Asp substitutions at residues S403, S404, S409 and S410 alter the LLPS behavior of TDP-43 LCD. In particular, unlike the LLPS of unmodified protein, LLPS of the phosphomimetic variants displays a biphasic dependence on salt concentration. Through coarse-grained modeling, we find that this biphasic salt dependence is derived from an altered mechanism of phase separation, in which LLPS-driving short-range intermolecular hydrophobic interactions are modulated by long-range attractive electrostatic interactions. Overall, this in vitro and in silico study provides a physiochemical foundation for understanding the impact of pathologically relevant C-terminal phosphorylation on the LLPS of TDP-43 in a more complex cellular environment.

Raza Haider and Brandon Shipley have contributed equally to this study.

KEYWORDS

amyotrophic lateral sclerosis, coarse-grained simulation, electrostatic forces, hydrophobic forces, liquid–liquid phase separation, TDP-43 phosphorylation

1 | INTRODUCTION

TAR DNA-binding protein of 43 kDa (TDP-43) is a nucleocytoplasmic nucleic-acid binding protein. Proteinaceous inclusions containing this protein typify a multitude of age-related neurodegenerative diseases, including amyotrophic lateral sclerosis, frontotemporal lobar degeneration, Alzheimer's disease, limbic predominant age-related TDP-43 encephalopathy and cerebral age-related TDP-43 with sclerosis (Arai et al., 2006; de Boer et al., 2020; Meneses et al., 2021; Neumann et al., 2006; Prasad et al., 2019). Previous studies have established that post-translational modifications such as N-terminal truncation, ubiquitination and phosphorylation may play an important role in the protein's misfolding and aggregation (Arai et al., 2006; Neumann et al., 2006; Neumann et al., 2009; Nonaka et al., 2009). Phosphorylation appears to be of particular importance in this regard, as proteinaceous inclusions are marked by hyperphosphorylated TDP-43 (Hasegawa et al., 2008; Neumann et al., 2009). Even though many TDP-43 phosphorylation sites have been identified (Eck et al., 2021), phosphorylation of residues in the intrinsically disordered low complexity domain (LCD; res. ∼267–414) appear to be especially strongly linked to disease (Eck et al., 2021; Hasegawa et al., 2008; Neumann et al., 2009; Neumann et al., 2021). Of these, four at the very C-terminal end of the protein (i.e., S403, S404, S409 and S410) are the best established, to the point that the presence of TDP-43 phosphorylated at these sites is an accepted biomarker of disease (Eck et al., 2021; Hasegawa et al., 2008; Neumann et al., 2009).

TDP-43 is comprised of four canonical domains—the N-terminal domain, which is involved in oligomerization of the protein, two RNA recognition motifs and the C-terminal, intrinsically disordered LCD (François-Moutal et al., 2019; Prasad et al., 2019). In the context of neurodegenerative diseases, the LCD has received particular attention, as patient-derived inclusions are enriched in C-terminal fragments containing this domain (Arai et al., 2006; Arseni et al., 2022; Igaz et al., 2008; Neumann et al., 2006). The LCD also appears to be critical for protein aggregation in experimental models (Furukawa et al., 2011; Johnson et al., 2009; Yang et al., 2010), and houses most of the disease-related mutations of TDP-43 (Buratti, 2015; Eck et al., 2021; Prasad et al., 2019). Furthermore, recent studies have revealed that the LCD is essential for liquid–liquid phase separation (LLPS) of TDP-43 (Carey & Guo, 2022; Conicella et al., 2016; Schmidt & Rohatgi, 2016), the phenomenon through which protein condenses into reversible, liquid-like droplets (Alberti & Dormann, 2019; Banani et al., 2017; Shin & Brangwynne, 2017). This is of particular interest since growing evidence points to a major role of LLPS in protein aggregation and the pathogenesis of age-related neurodegenerative diseases (Alberti & Dormann, 2019; Babinchak & Surewicz, 2020; Haider et al., 2023; Wang et al., 2021; Zbinden et al., 2020).

LLPS of the TDP-43 LCD is believed to be driven by multiple intermolecular forces working in concert. Among those, hydrophobic interactions between multiple non-polar residues (Babinchak et al., 2019; Babinchak et al., 2020; Li, Chen, et al., 2018; Schmidt et al., 2019) as well interactions involving aromatic side chains (e.g., cation-π, π-π stacking) (Li, Chiang, et al., 2018; Mohanty et al., 2023; Schmidt et al., 2019) appear to be especially important, since addition of compounds that disrupt hydrophobic forces and removal of key Trp and Phe residues severely inhibit LLPS. Of equal importance appears to be the transiently α-helical region, a segment within the LCD encompassing residues ∼320–340. Indeed deletion of this segment or helix-breaking mutations within it lead to the abolition of protein LLPS (Conicella et al., 2016; Haider et al., 2024; Jiang et al., 2013; Li, Chen, et al., 2018; Li, Chiang, et al., 2018; Schmidt et al., 2019; Schmidt & Rohatgi, 2016). On the other hand, electrostatic interactions between the relatively few charged residues natively present within the LCD (concentrated mainly within the N-terminal part of the protein) result in repulsive intermolecular electrostatic forces between monomers, leading to inhibition of LLPS at low ionic strength (Babinchak et al., 2019; Li, Chen, et al., 2018).

The balance of these forces is likely to be substantially impacted by specific post-translational modifications. However, little information is available in this regard, especially for TDP-43 phosphorylated at pathologically critical sites within the C-terminal part of the LCD. Here we attempt to bridge this gap using a phosphomimetic approach in which Ser residues at position 403, 404, 409 and 410 have been replaced with Asp. Our experimental data reveal that these phosphomimetic substitutions alter the LLPS behavior of TDP-43 LCD, especially its dependence on ionic strength. Coarse-grained

simulations provide insight into the mechanism of this altered behavior, suggesting that it is due to a different balance of hydrophobic and electrostatic forces in the non-modified and phosphomimetic proteins.

2 | RESULTS

2.1 | C-terminally phosphomimetic substitutions confer a biphasic salt dependence to TDP-43 LCD LLPS

To investigate how phosphorylation of C-terminal Ser residues (i.e., S403, S404, S409 and S410) in TDP-43 LCD affects protein LLPS, we generated phosphomimetic variants of the LCD, with varying numbers of Ser-to-Asp substitutions to model phosphorylation at two (S403D/S404D, referred to as 2-PM TDP-43; +1 predicted net charge) or four (S403D/S404D/S409D/S410D, referred to as 4-PM TDP-43; −1 predicted net charge) of the aforementioned C-terminal residues (Figure 1a). We then measured the turbidity (the optical density at 600 nm) of these variants at 20 μM concentration and physiological pH as a function of NaCl concentration to see the effect of these C-terminal phosphomimetic substitutions on TDP-43 LCD LLPS. Wild-type (WT) TDP-43 LCD LLPS showed a direct dependence on ionic strength, with increasing salt concentration promoting phase separation monotonically, in agreement with other studies (Babinchak et al., 2019; Conicella et al., 2016; Li, Chiang, et al., 2018). LLPS of the phosphomimetic TDP-43 LCD proteins, in contrast, was characterized by a biphasic salt dependence. At low-to-moderate NaCl concentrations, 2-PM TDP-43 LCD and 4-PM TDP-43 LCD showed diminished LLPS in response to increasing ionic strength, opposite of the behavior of WT protein. However, at moderate-to-high NaCl concentrations, 2-PM TDP-43 LCD and 4-PM TDP-43 LCD showed increased LLPS in response to increasing ionic strength; this switch occurred at a different salt concentration for each phosphomimetic variant (Figure 1b,c). Furthermore, the droplets formed by 4-PM TDP-43 LCD were also much smaller than those formed by the other proteins (Figure 1c).

In order to more fully document these surprising results, saturation concentrations (c_{sat}) were calculated and protein concentration versus salt concentration phase diagrams were constructed for all of the TDP-43 LCD variants (Figure 2a,b). The phase diagrams substantiated the non-monotonic salt dependences of the phosphomimetic proteins' LLPS, illustrating that the concentrations of protein at which phase separation was observed at first increased with increasing ionic strength, and then decreased as ionic strength was increased further (Figure 2b). This behavior was reflected in the trends of the saturation concentrations (Figure 2a). The salt concentration range in which the LLPS of a given phosphomimetic variant had an inverse dependence on ionic

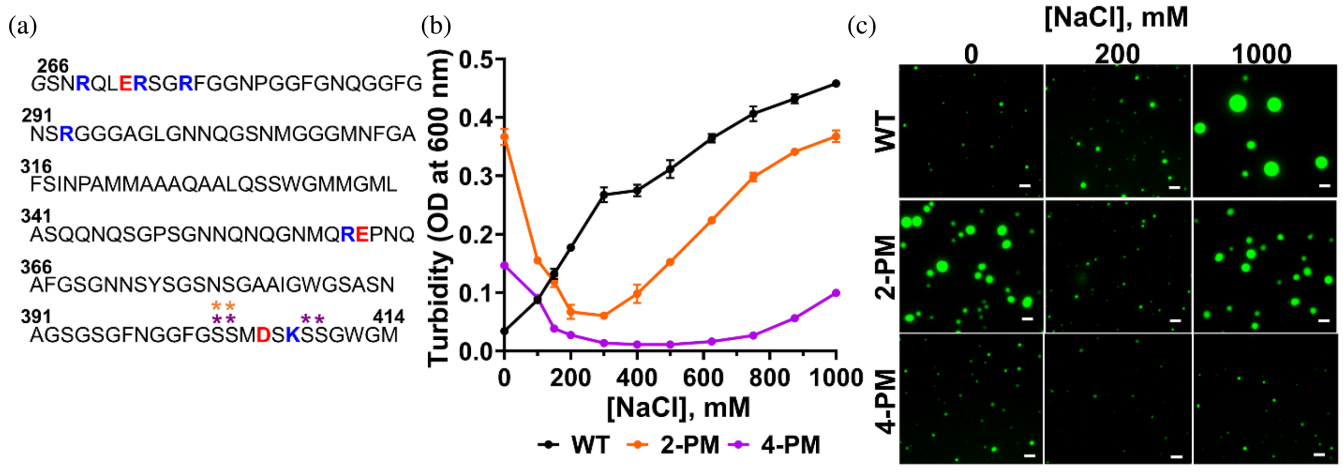

FIGURE 1 The LLPS of C-terminal phosphomimetic TDP-43 LCD variants shows a non-monotonic salt response. (a) Sequence of the TDP-43 low complexity domain construct used in this study. An extra N-terminal glycine from the purification process is *italicized*, and natively positively and negatively charged residues are marked in blue and red, respectively. The residues that were phosphomimetically substituted to form the 2-PM variant are marked with orange asterisks, and those of the 4-PM variant are marked with purple asterisks. (b) Turbidity plots of TDP-43 LCD variants (20 μM in each case) as a function of ionic strength. Error bars represent SD ($n = 3$). (c) Representative fluorescence microscopy images of TDP-43 LCD variants at 20 μM protein. Proteins were labeled with Alexa Fluor 488, and the ratio of labeled-to-unlabeled protein was 1:20 for each protein. Scale bar, 3 μm. Experiments were performed in 20 mM potassium phosphate buffer (pH 7.4), and data/images were collected ~20 min after sample preparation. OD, optical density.

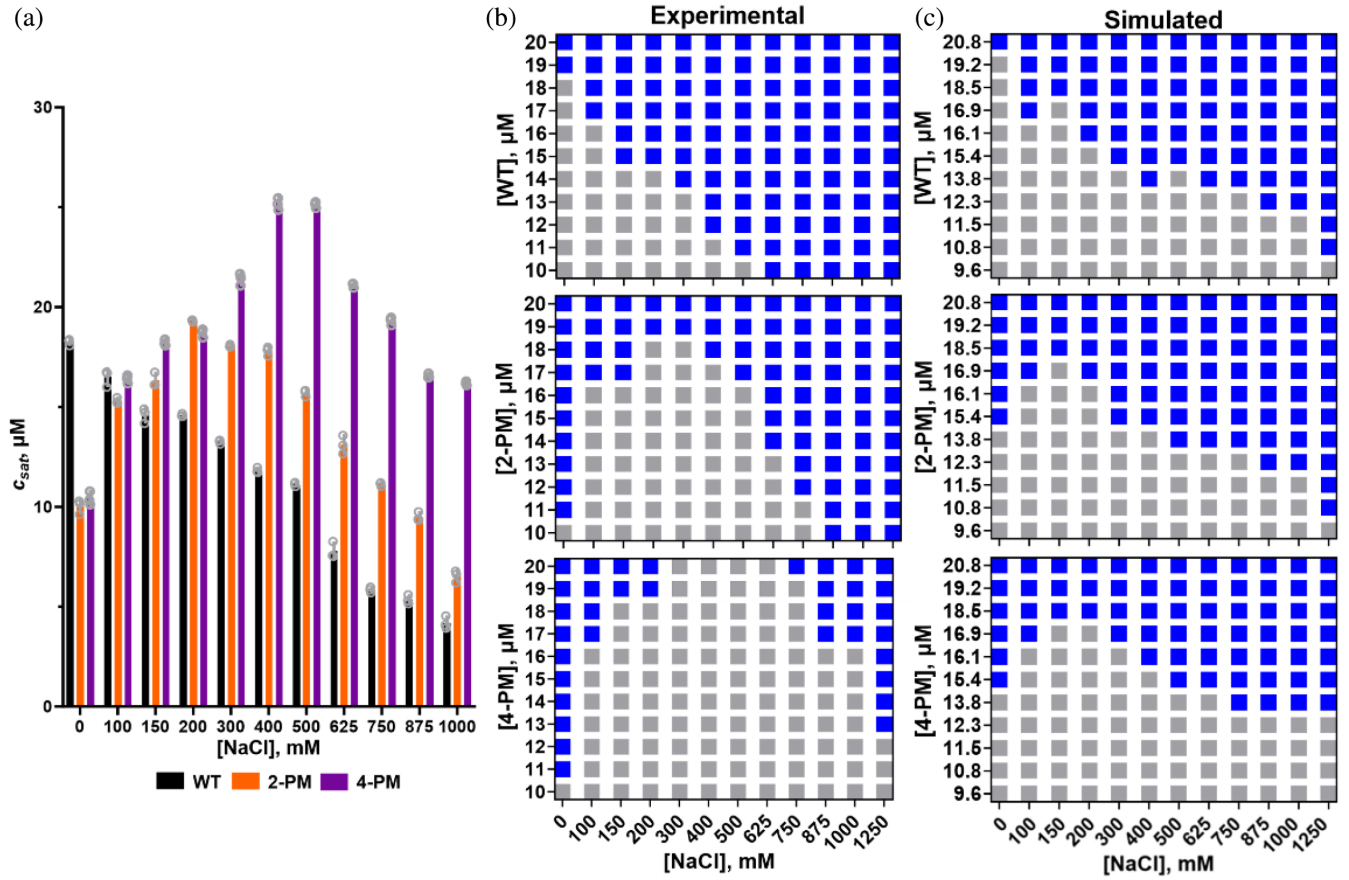

FIGURE 2 Phase diagrams and saturation concentrations of TDP-43 LCD variants. (a) Experimentally determined saturation concentrations for TDP-43 LCD variants. Error bars represent SD ($n = 3$), and gray circles represent each replicate. (b) Experimentally determined phase diagrams (from data run in triplicate). (c) In silico phase diagrams (from data run in duplicate). The experiments and the in silico simulations were performed in 20 mM potassium phosphate buffer (pH 7.4), at room temperature. Gray and blue squares indicate the absence and presence of LLPS, respectively.

strength was denoted its "low salt regime," and the range in which it showed a direct dependence on ionic strength was denoted its "high salt regime."

2.2 | Hydrophobic forces drive TDP-43 LCD phase separation

A number of intermolecular forces have been shown to contribute to WT TDP-43 LCD LLPS. The LCD is enriched in hydrophobic amino acids, and hydrophobic interactions between these residues have a key role in driving the protein's phase separation (Babinchak et al., 2019; Babinchak et al., 2020; Li, Chen, et al., 2018; Schmidt et al., 2019). A segment of the LCD spanning residues ~320–340 that has high propensity to form a transient α-helix has been revealed to be especially important, as it mediates intermolecular helix–helix contacts without which LLPS is abrogated (Conicella et al., 2016; Haider et al., 2024; Jiang et al., 2013; Li, Chen, et al., 2018; Li, Chiang, et al., 2018; Schmidt et al., 2019; Schmidt & Rohatgi, 2016). Additionally, there is evidence that repulsive intermolecular electrostatic interactions arising from the net +3 charge of the protein (concentrated mainly at its N-terminal end) are at play, inhibiting LLPS at low salt concentrations (Babinchak et al., 2019; Li, Chen, et al., 2018). The biphasic salt response observed for LLPS of the C-terminal phosphomimetic variants, however, suggested that electrostatic forces may drive condensation of these variants in the low salt regime, and hydrophobic forces take over in the high salt regime.

To investigate the roles of electrostatic and hydrophobic forces in the phase separation of C-terminally phosphomimetic TDP-43 LCD, we set up sequence-dependent coarse-grained simulations. Our methods were based on established techniques, which have previously been used to study LLPS of TDP-43 LCD (Gruijs da Silva et al., 2022), as well as that of other proteins such as the LCD of the RNA-binding protein FUS (Dignon

et al., 2018; Joseph et al., 2021; Monahan et al., 2017), the DEAD-box helicase LAF-1 (Dignon et al., 2018) and the RNA-binding protein hnRNPA2 (Ryan et al., 2018). In our approach, amino acids were represented as spheres with effective masses, charges, hydrophobicities and sizes taken from the literature (Table S1) (Dignon et al., 2018). A Yukawa screened Coulombic potential and a modified Lennard-Jones potential of the Ashbaugh-Hatch functional form (Ashbaugh & Hatch, 2008) were used to implement electrostatic and hydrophobic forces, respectively. To verify that the proposed coarse-grained simulation framework produced meaningful results, we generated simulated phase separation diagrams ($N = 2$ duplicates) and compared them to experimentally determined phase diagrams. Though there were some quantitative differences between the experimental and simulated data in terms of the saturation concentrations of the proteins and the salt concentrations at which LLPS of the phosphomimetic variants transitioned from an inverse salt dependence to a direct salt dependence, the simulated phase diagrams verified that the coarse-grained model captured the biphasic salt dependence the LLPS of the phosphomimetic variants displayed in our experiments in vitro. The non-monotonic salt dependences of the phosphomimetic proteins were recapitulated within a similar protein concentration range as observed in the experiments, as was the monotonic salt dependence of the WT protein (Figure 2b,c). Considering the unavoidable approximation used in coarse-grained simulations, such a good correspondence between experimental and simulated phase diagrams is quite remarkable, validating our in silico model. To achieve these results, the well depth (ε) of the modified Lennard-Jones potential was explicitly made to scale incrementally with ionic strength (0.1985–0.205 $\frac{\text{kcal}}{\text{mol}}$ from 0 to 1250 mM NaCl) so as to represent the kosmotropic nature of Na+ ions and the inherent salt dependence of hydrophobic forces (Moelbert et al., 2004). In the absence of this perturbation, simulated phase separation diagrams notably did not recapitulate the qualitative trends of their experimental counterparts (Figure S1). Of note, while we account for salt-dependent hydrophobic interactions using an adjustment of the modified Lennard-Jones potential well depth (ε), another study has accounted for this effect by adjusting the hydrophobicity parameter (λ) (Wohl et al., 2021). When comparing the two models, it was found that they produce qualitatively similar results (Figure S2 and Table S2).

Using the in silico data, we next compared how the total intermolecular electrostatic force changed for each TDP-43 variant at one selected protein concentration (20.8 μM) as the protein transitioned from the low to the high salt regime. Our analysis focused on the 20.8 μM simulations because, at this protein concentration, all three LCD variants phase separated at all salt concentrations tested in silico (Figure 2c). The data showed that WT protein experienced a net repulsive electrostatic force at 0 mM NaCl that weakened as ionic strength was increased (Figure 3a), in line with expectations as WT TDP-43 LCD has a net positive charge (of +3). The phosphomimetic variants, in contrast, experienced a net attractive electrostatic force at 0 mM NaCl (which also weakened as ionic strength was increased) (Figures 3a and S3), even though 2-PM TDP-43 and 4-PM TDP-43 also have non-zero net charges (of +1 and −1, respectively). This attractive electrostatic force likely arose from the polarized charge distributions of the phosphomimetic proteins. Unlike WT TDP-43, which has only a positively charged N-terminal region, 2-PM TDP-43 and 4-PM TDP-43 have both the native N-terminal "positive pole" and a C-terminal "negative pole" (Figures 1a and 3b), which could interact intermolecularly to generate the attractive electrostatic forces experienced by the phosphomimetic proteins in the low salt regime.

To test whether the charge distributions of the phosphomimetic variants played a part in the biphasic LLPS behavior they exhibited, we introduced two charge-attenuating mutations (R275Q/R293Q) to the TDP-43 LCD. This WT+R275Q/R293Q TDP-43 variant had the same net charge (+1) as 2-PM TDP-43, but no polarized charge distribution, and indeed its LLPS did not show a convincing biphasic salt dependence (Figure S4). Taken together, these results at first suggested that the inverse salt dependence exhibited by the phosphomimetic TDP-43 variants could be due to attractive electrostatic forces driving their LLPS in their low salt regimes, and that the reversal of this relationship in the high salt regimes may be because the increased ionic strength screened out the electrostatic forces and allowed hydrophobic forces to take over.

Examining the total intermolecular hydrophobic forces, however, cast some doubt regarding the importance of electrostatic forces in TDP-43 phase separation. Indeed, for each protein at every salt concentration surveyed, the total hydrophobic force exceeded the total electrostatic force by two orders of magnitude (Figures 3a and 4a). Furthermore, at 0 mM NaCl, the total hydrophobic forces experienced by the phosphomimetic TDP-43 variants were stronger than that experienced by WT protein (Figure 4a). This analysis indicated that hydrophobic forces were a major driver of LLPS of not only WT TDP-43, but also of 2-PM TDP-43 and 4-PM TDP-43, in both the low salt and high salt regimes. To experimentally test this simulation-suggested possibility, we formed droplets of all protein variants studied in 0 mM NaCl, where electrostatic forces would be at their strongest, and exposed

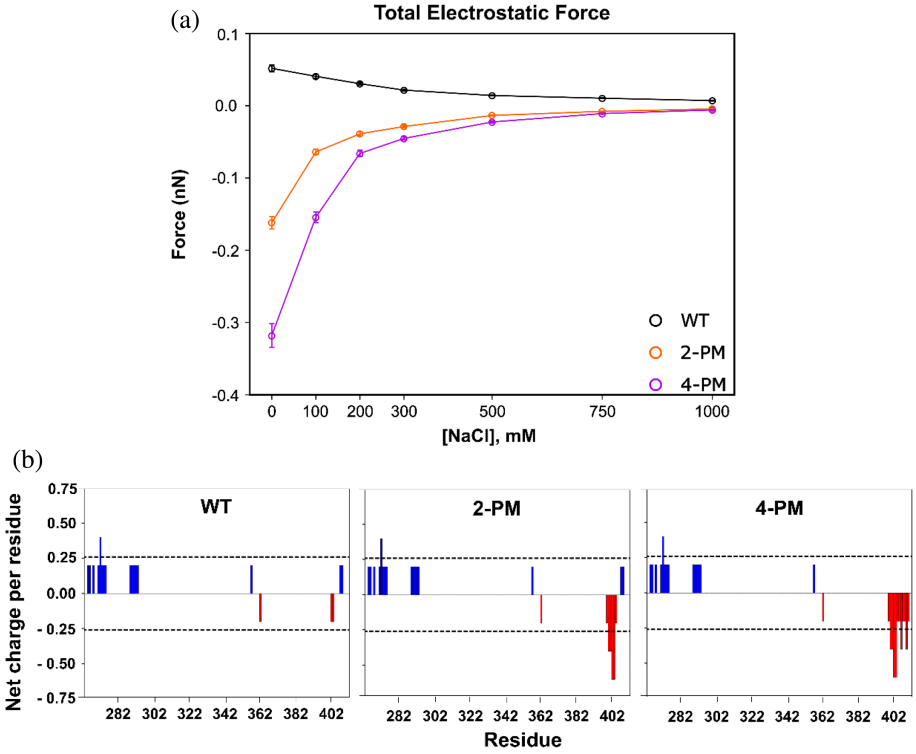

FIGURE 3 Total intermolecular electrostatic force generated by TDP-43 LCD interactions for each variant under the conditions of phase separation. (a) Sum of total intermolecular electrostatic forces acting on TDP-43 LCD variants as a function of salt concentration, derived from simulations of 20.8 μM protein. Error bars are SD, derived via block bootstrapping. (b) Net charge per residue plots for TDP-43 LCD variants, generated using the CIDER tool. Charge was calculated over a five residue window.

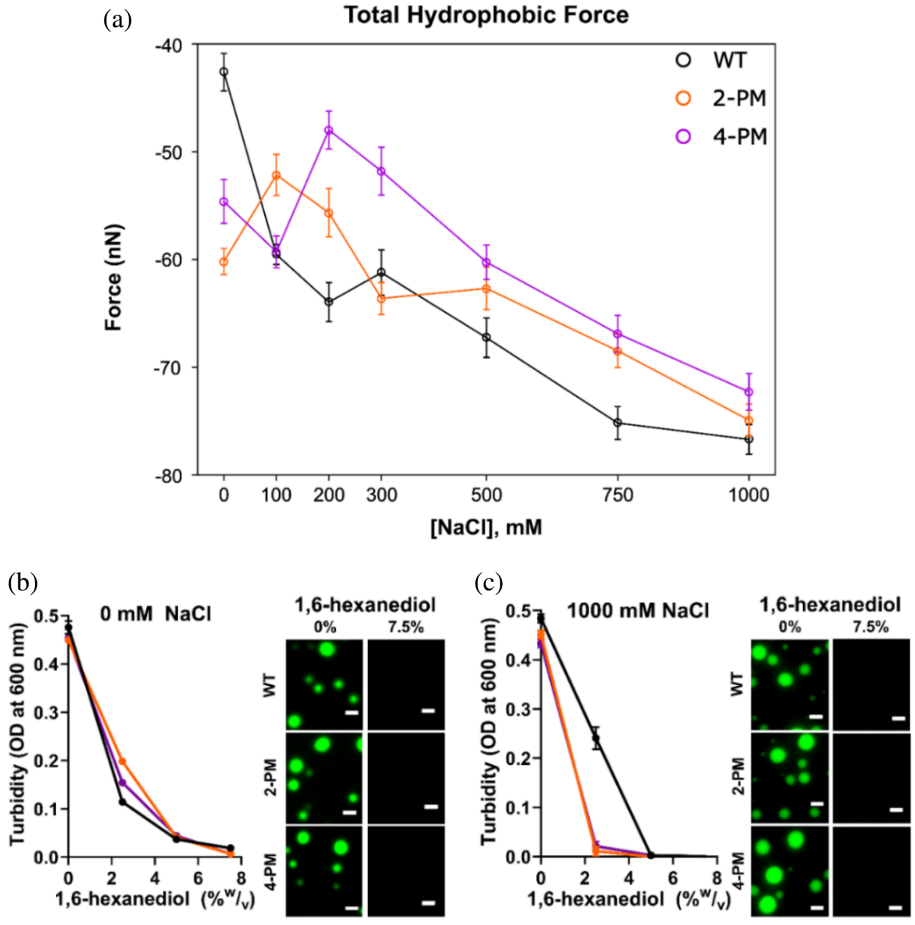

FIGURE 4 Hydrophobic forces dominate LLPS of WT TDP-43 LCD and phosphomimetic TDP-43 LCD in both the low salt and high salt regimes. (a) Sum of total intermolecular hydrophobic forces acting on TDP-43 LCD variants as a function of salt concentration, derived from simulations at a protein concentration of 20.8 μM. Error bars are SD, derived via block bootstrapping. (b) Sensitivity of TDP-43 droplets formed at 0 mM NaCl to 1,6-hexanediol, as shown by turbidity (*left*) and representative microscopy images (*right*). (c) Sensitivity of TDP-43 droplets formed at 1000 mM NaCl to 1,6-hexanediol, as shown by turbidity (*left*) and representative microscopy images (*right*). Proteins were labeled with Alexa Fluor 488, and the ratio of labeled-to-unlabeled protein was 1:20 for each protein. Scale bar, 3 μm. Experiments were performed in 20 mM potassium phosphate buffer (pH 7.4), and data/images were collected ~20 min after sample preparation. OD, optical density. Error bars represent SD ($n = 3$).

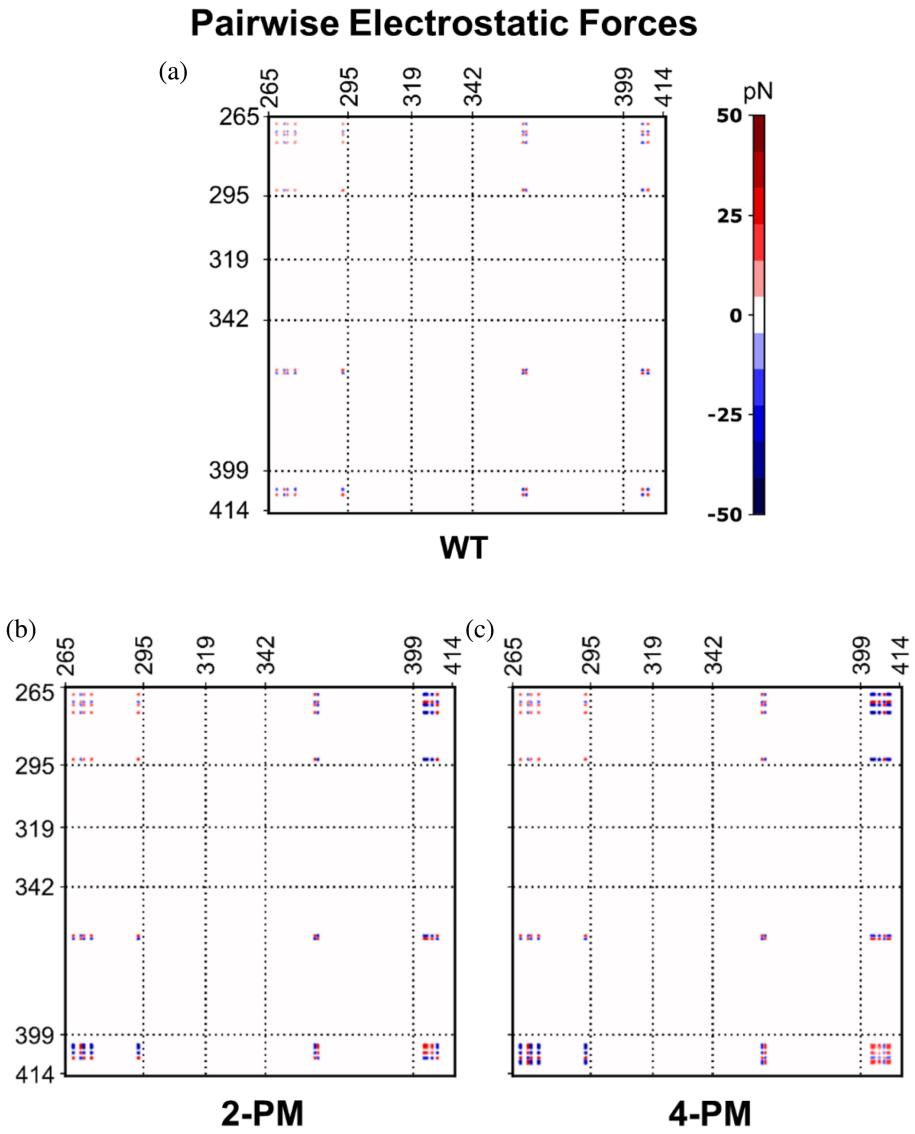

FIGURE 5 Intermolecular residue-residue pairwise electrostatic force plots of phase-separated TDP-43 LCD variants in the absence of salt. Pairwise intermolecular electrostatic forces of (a) WT TDP-43 LCD, (b) 2-PM TDP-43 LCD and (c) 4-PM TDP-43 LCD. Data were generated from simulations at a protein concentration of 20.8 μM in a buffer containing no NaCl. Dashed reference lines mark the same residues in all three plots.

them to 1,6-hexanediol, an aliphatic alcohol that disrupts hydrophobic interactions (Kroschwald et al., 2015). 1,6-hexanediol did, in fact, dissolve these droplets (Figure 4b), just as it did droplets formed at 1000 mM NaCl (Figure 4c), supporting the notion that hydrophobic forces were major drivers of phase separation for all three proteins regardless of ionic strength.

2.3 | Electrostatic forces tune the hydrophobic forces driving phosphomimetic TDP-43 LCD LLPS

Though inspecting the total intermolecular electrostatic and hydrophobic forces revealed that the latter were a major driver of phase separation of WT TDP-43 and phosphomimetic TDP-43 at all salt concentrations tested, this finding did not explain the inverse salt dependences of 2-PM TDP-43 LLPS and 4-PM TDP-43 LLPS in their low salt regimes. Due to the kosmotropic nature of Na+ ions (Moelbert et al., 2004), NaCl enhances the hydrophobic effect, and would theoretically promote hydrophobic forces. The observation that NaCl inhibited LLPS of phosphomimetic TDP-43 in the low salt regime, however, suggested that electrostatic interactions still played a significant role. To explore this apparent conundrum, we constructed plots of the pairwise intermolecular electrostatic and hydrophobic forces occurring between every pair of residues of each protein at 0 mM NaCl (firmly in the low salt regime), 200 mM NaCl (near the transition point between the low and high salt regimes of 2-PM and 4-PM TDP-43) and 1000 mM NaCl (firmly in the high salt regime) (Figures 5, 6 and S3). This analysis allowed us to understand how electrostatic and hydrophobic interactions between different regions of the proteins contributed to LLPS across the low and high salt regimes.

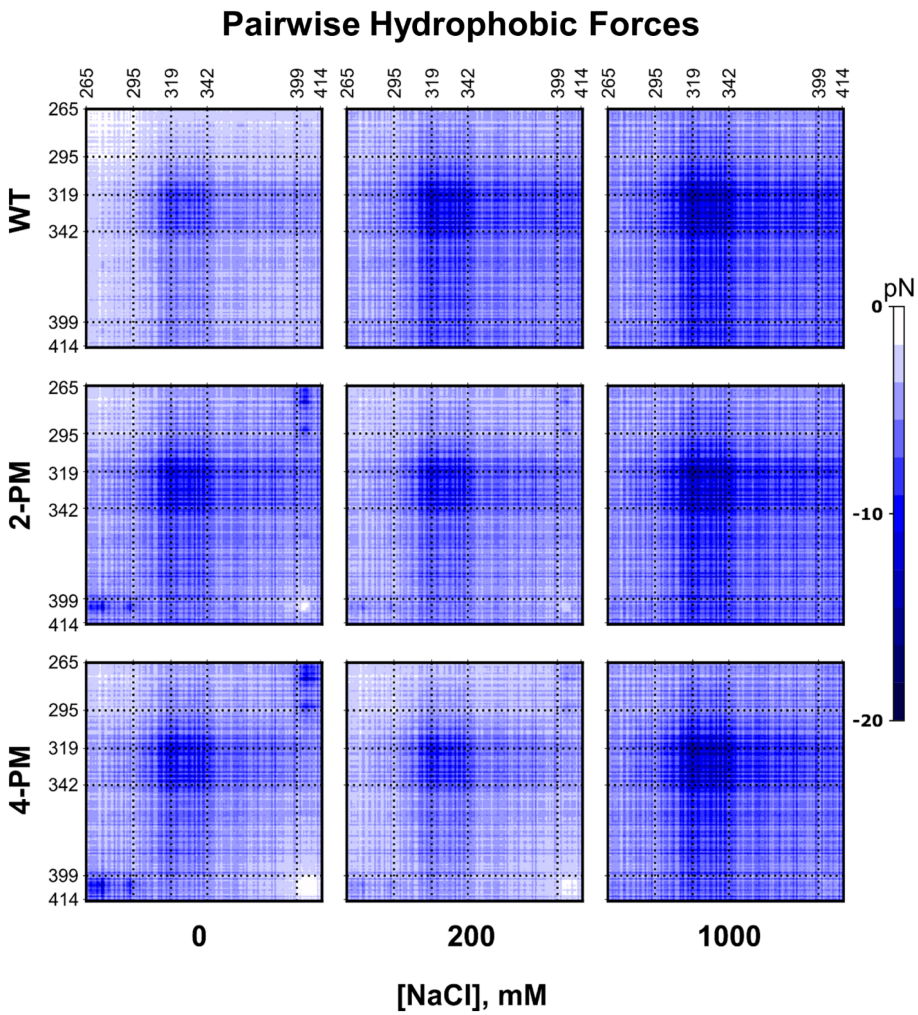

FIGURE 6 Intermolecular residue-residue pairwise hydrophobic force plots of phase-separated TDP-43 LCD variants. Pairwise intermolecular hydrophobic forces of WT TDP-43 LCD (*Top*), 2-PM TDP-43 LCD (*Middle*) and 4-PM TDP-43 LCD (*Bottom*) at various ionic strengths. Data were generated from simulations at a protein concentration of 20.8 μM. Dashed reference lines mark the same residues in all nine plots.

Interestingly, our simulations at 0 mN NaCl revealed that individual electrostatic forces were of the same order of magnitude as individual hydrophobic forces (Figures 5 and 6). Thus, it appeared that the vastly larger magnitude of the total intermolecular hydrophobic force as compared to total intermolecular electrostatic force for each protein in the low salt regime (Figures 3a and 4a) was largely due to the paucity of residues that were charged (8–12 residues) versus those able to interact hydrophobically (151 residues), rather than individual electrostatic forces being weaker than individual hydrophobic forces. Additionally, the pairwise electrostatic force data confirmed that the phosphomimetic proteins experienced net electrostatic repulsion between N-/N-terminals and C-/C-terminals, as well as net electrostatic attraction between N-/C-terminals. On the other hand, WT protein only experienced net electrostatic repulsion between N-/N-terminals (Figures 5 and S3). Hydrophobic forces are exquisitely sensitive to distance, showing sharp exponential decay as the distance between interacting hydrophobic surfaces is enlarged. While ionically screened electrostatic forces also decay exponentially as the distance between interacting particles is increased, this decay is generally less prominent relative to hydrophobic forces at low salt concentrations (Israelachvili & Pashley, 1982). Thus, any electrostatic interaction that brings hydrophobic surfaces closer together would result in a stronger hydrophobic force between them. Conversely, any electrostatic interaction that pushes the surfaces farther apart would weaken said hydrophobic force. The pairwise hydrophobic force plots demonstrated this was indeed the case. At 0 mM NaCl, the pairwise hydrophobic forces from C-/C-terminal interactions were stronger for WT protein, which had no significant electrostatic forces between these regions, than for the phosphomimetic proteins, which had repulsive electrostatic forces between these regions. On the other hand, the pairwise hydrophobic forces from N-/C-terminal interactions were weaker for WT TDP-43 compared to those of 2-PM TDP-43 and 4-PM TDP-43, in accordance with the corresponding electrostatic forces being negligible for the former and attractive for the latter at this ionic strength.

The modulatory effect of electrostatic forces on the hydrophobic forces driving phosphomimetic TDP-43

LLPS was also evident as ionic strength was increased. For WT protein, as NaCl concentration was increased from 0 to 200 to 1000 mM, the pairwise intermolecular hydrophobic forces became stronger. For the 2-PM and 4-PM variants, in contrast, the pairwise intermolecular hydrophobic forces became weaker from 0 to 200 mM NaCl, but became stronger from 200 to 1000 mM NaCl. In fact, at 1000 mM NaCl, the phosphomimetic proteins' plots were practically indistinguishable from that of the WT protein (Figure 6). Evidently, protein molecules within liquid-like droplets of WT TDP-43 LCD packed differently than those withing droplets of 2-PM and 4-PM variants in the low-salt regime. Hydrophobic N-/C-terminal interactions were much more prominent and stable in the cases of the variants, whereas there was nearly complete abrogation of hydrophobic C-/C-terminal interactions. However, as NaCl concentration was increased sufficiently the phosphomimetic proteins entered their high-salt regimes, the effects of electrostatic interactions on the liquid-like structures was diminished, and all of the protein variants appeared to pack similarly within droplets.

Taken together, these results indicated a potential mechanism for the biphasic salt response of phosphomimetic TDP-43 LLPS. For WT protein, salt strengthened the hydrophobic forces mediating LLPS in a two-fold manner: (i) by enhancing the hydrophobic effect due to its kosmotropic nature and (ii) by screening repulsive N-/N-terminal electrostatic interactions. For the phosphomimetic variants, on the other hand, these two effects did not work in concert. While increasing NaCl concentration still enhanced the hydrophobic effect, the attractive N-/C-terminal electrostatic interactions that promoted hydrophobic forces driving LLPS were reduced. This led to overall weaker hydrophobic forces and inhibited LLPS for 2-PM TDP-43 LCD and 4-PM TDP-43 LCD as NaCl concentration was increased in the low salt regime. In the high salt regime, however, electrostatic forces were completely screened out; thus increasing ionic strength solely strengthened the hydrophobic forces (and thus LLPS), mirroring the behavior of WT protein.

2.4 | The transiently α-helical region of TDP-43 remains essential for LLPS of C-terminally phosphomimetic variants of TDP-43 LCD

The pairwise hydrophobic force plots for WT TDP-43, 2-PM TDP-43 and 4-PM TDP-43 all showed that the strongest hydrophobic forces experienced by the proteins in their phase separated states were generated by a stretch of amino acids interacting intermolecularly with itself (Figure 6). This stretch, which encompassed residues ~317–342, roughly corresponded to the transiently α-helical region of TDP-43. Thus, it appeared that, akin to the WT protein (Conicella et al., 2016; Jiang et al., 2013; Li, Chen, et al., 2018; Li, Chiang, et al., 2018; Schmidt et al., 2019; Schmidt & Rohatgi, 2016), the transiently α-helical region was also of key importance for LLPS of the phosphomimetic variants.

To further explore this issue, we resorted to the A326P LCD variant, in which the transiently α-helical structure is known to be largely disrupted, as previously demonstrated by NMR studies (Conicella et al., 2016). Consistent with this notion, the far-UV CD spectrum of this variant was characterized by a substantially lower $\lambda_{220}/\lambda_{200}$ nm dichroic ratio, whereas the spectra of WT TDP-43 LCD and 4-PM TDP-43 LCD were nearly identical (Figure 7a), strongly suggesting the quadruple phosphomimetic substitutions within the 4-PM variant did not affect the structure of the transiently α-helical region.

The A326P point mutation was shown in previous studies to abolish LLPS of WT TDP-43 LCD (Conicella et al., 2016; Conicella et al., 2020), which we recapitulated in our own experiments. Furthermore, this helix-breaking mutation completely abrogated condensation of 4-PM TDP-43 LCD under conditions where this phosphomimetic variant without the mutation formed liquid-like droplets (Figure 7b). Thus, akin to the case of the WT protein, the transiently α-helical region appeared to be necessary for LLPS of the phosphomimetic variant. Finally, we introduced the W334G mutation to 4-PM TDP-43 LCD; this mutation removes a tryptophan residue previously shown to be vital to WT TDP-43 LCD LLPS, while leaving the transiently α-helical structure intact (Li, Chiang, et al., 2018). W334G 4-PM protein was not able to phase separate under the tested conditions (Figure 7c). Taken together, these results strongly suggested that the transiently α-helical region and key residues therein, which are crucial for LLPS of the WT protein, were still required for the phase separation of C-terminally phosphomimetic TDP-43 LCD.

3 | DISCUSSION

Much of the TDP-43 within the inclusions that characterize age-related neurodegenerative diseases such as amyotrophic lateral sclerosis (ALS), frontotemporal lobar degeneration (FTLD), limbic-predominant age-related TDP-43 encephalopathy and cerebral age-related TDP-43 with sclerosis is post-translationally modified (Arai et al., 2006; Neumann et al., 2006; Neumann et al., 2009; Nonaka et al., 2009). For example, ubiquitination and N-terminal truncation of TDP-43 have been extensively

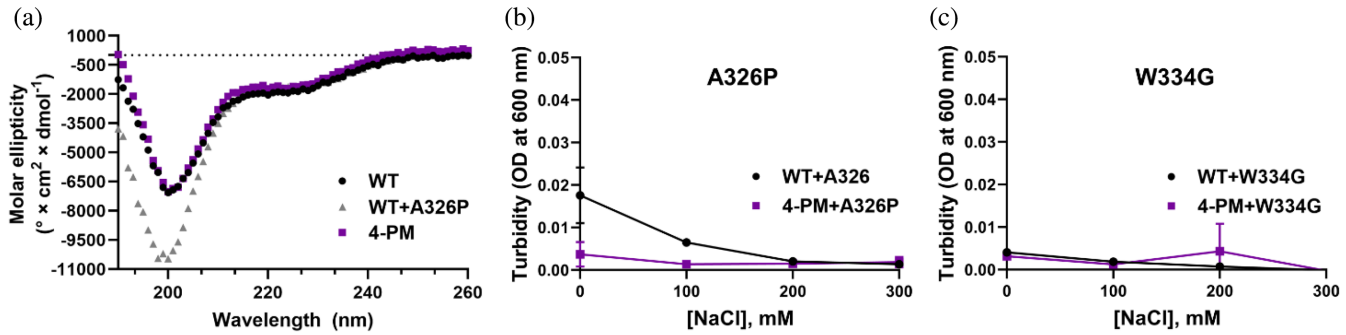

FIGURE 7 The transiently α-helical region remains critical for LLPS of phosphomimetic TDP-43 LCD variants. (a) Far-UV circular dichroism spectra of WT and 4-PM TDP-43 LCD. (b, c), Turbidity plots for WT and 4-PM TDP-43 LCD with the helix-breaking A326P mutation (b) and the aromatic-residue-removing W334G mutation (c). All experiments were done at room temperature, pH 7.4. OD, optical density. Error bars represent SD ($n = 3$).

observed, with C-terminal fragments containing the low complexity domain (LCD) of the protein being a major component of amyloid aggregates in ALS and FTLD (Arai et al., 2006; Neumann et al., 2006; Nonaka et al., 2009). Phosphorylation, though, is of particular significance. Not only has phosphorylated TDP-43 been shown to segregate specifically to the inclusions that serve as hallmarks of TDP-43 proteinopathy, but phosphorylation at certain C-terminal residues (e.g., S403, S404, S409 and S410) is so widespread in pathology that it is used as a biomarker of disease (Eck et al., 2021; Hasegawa et al., 2008; Neumann et al., 2009). There is evidence that phosphorylation may be causative of proteinopathy, as studies have shown that it can reduce TDP-43 splicing activity and promote cytoplasmic mislocalization of protein; in cellular and animal models, phosphorylated TDP-43 has even been shown to exert several neurotoxic effects, resulting in motor dysfunction and increased cell death (Eck et al., 2021). Other studies, however, have suggested that TDP-43 phosphorylation may be neuroprotective, providing evidence that this post-translational modification slows down aggregation, or may simply be a byproduct of disease (e.g., an attempt by protein quality control machinery to re-solubilize aggregated proteins) (Eck et al., 2021; Haider et al., 2023; Haider et al., 2024). Ultimately, resolution of this controversy will require further study, especially regarding the effects of phosphorylation at specific TDP-43 sites and the temporal relationship between this post-translational modification and aggregation. As such, the role of phosphorylation in the development of TDP-43 proteinopathies is an active area of investigation. One topic within this field that remains largely unexplored, however, is the effect of C-terminal phosphorylation on TDP-43 liquid–liquid phase separation (LLPS). TDP-43 forms membraneless condensates through the mechanism of LLPS, which is driven by its LCD (Alberti & Dormann, 2019; Banani et al., 2017; Carey & Guo, 2022; Conicella et al., 2016; Schmidt & Rohatgi, 2016; Shin & Brangwynne, 2017), and ever-mounting evidence has linked dysregulation of phase separation to disease (Alberti & Dormann, 2019; Babinchak & Surewicz, 2020; Haider et al., 2023; Wang et al., 2021; Zbinden et al., 2020). The relative dearth of studies investigating how this potentially pathogenic process is affected by C-terminal phosphorylation, therefore, represents a crucial gap in our understanding of TDP-43 proteinopathies. To address this issue, we employed a combination of experimental and coarse-grained simulation-based approaches to ascertain the impact of these post-translational modifications on TDP-43 LCD condensation using a phosphomimetic model of the protein's low-complexity domain.

Akin to many other LLPS-prone low complexity domains, the condensation of TDP-43 LCD is promoted by increasing the ionic strength of the buffer (Babinchak et al., 2019; Haider et al., 2023; Martin et al., 2021; Murthy et al., 2019). This is likely due to strengthening of short-range intermolecular hydrophobic interactions as well as weakening of repulsive, long-range intermolecular electrostatic interactions (Babinchak et al., 2019; Babinchak et al., 2020; Li, Chen, et al., 2018; Schmidt et al., 2019). While our present study fully confirmed this salt-dependence of WT TDP-43 LCD LLPS, it also revealed that the LLPS behavior of the phosphomimetic variants studied is dramatically different. First, in the absence of NaCl, both 2-PM TDP-43 LCD and 4-PM TDP-43 LCD phase separated to a greater extent than the WT protein. These results were unexpected, as another group previously suggested (based on coarse-grained simulations only, without experimental data) that C-terminal phosphomimetic substitutions suppressed LLPS of the TDP-43 LCD (Gruijs da Silva et al., 2022). In their study, however, the simulations were run at 150 mM NaCl,

whereas our data covered a broad range of ionic strengths (0–1250 mM NaCl). Second, in sharp contrast to the WT protein, LLPS of the phosphomimetic variants exhibited a biphasic response to ionic strength, first decreasing at relatively low salt concentrations and then increasing as NaCl concentration was increased above a certain threshold level.

Interestingly, LLPS of unmodified, full-length TDP-43, which has several additional folded domains that interact with the LCD to modulate phase separation (Haider et al., 2023), was also reported to have a biphasic salt dependence (Krainer et al., 2021); similar behavior was observed for full-length FUS, another RNA-binding protein associated with age-related neurodegenerative diseases (Haider et al., 2023; Krainer et al., 2021). The non-monotonic relationship between the LLPS of these proteins and ionic strength was ascribed to attractive electrostatic intermolecular forces primarily driving phase separation in their low salt regimes, and attractive hydrophobic intermolecular forces taking over in their high salt regimes (Krainer et al., 2021). At first, this mechanism appeared congruent with the results for our TDP-43 LCD phosphomimetic variants as well, particularly given that the C-terminal phosphomimetic substitutions created polarized charge distributions in the 2-PM and 4-PM proteins that could lead to attractive electrostatic protein–protein interactions.

To test this potential mechanism, we employed a coarse-grained simulation framework. Although coarse-grained modeling does not provide the same resolution as atomistic modeling, these simulations allowed us to explore a large number of salt/protein concentration combinations on a realistic timescale. To further increase computational efficiency, we used a relatively small number of proteins ($N \leq 54$) for each simulation in a box with periodic boundary conditions. This, however, did not appear to affect the accuracy of our results, as they showed the same trends as those generated by simulations run with five times the number of proteins, albeit with minor quantitative differences (Figure S5). TDP-43 LCD LLPS involves many types of interactions, including those based on aromatic residues (e.g., cation-π, π-π stacking) (Babinchak et al., 2019; Babinchak et al., 2020; Li, Chen, et al., 2018; Li, Chiang, et al., 2018; Mohanty et al., 2023; Schmidt et al., 2019). Given the difficulties in directly including some of these interactions in coarse-grained simulations, in our framework we explicitly modeled only electrostatic interactions (via a Yukawa screened Coulombic potential) and hydrophobic interactions (via the attractive portion of a modified Lennard-Jones potential). The quantitative differences observed between the simulated and experimental data (primarily in terms of saturation concentrations and the transition point between the low salt and high salt regimes of the phosphomimetic variants) are likely the results of this streamlined approach. Such simplifications notwithstanding, our simulation framework generated phase diagrams that matched all of the qualitatively important features seen in their experimental counterparts, including the monotonic and biphasic salt dependences of WT and phosphomimetic TDP-43 LCD LLPS, respectively, and the relative LLPS-propensities of the phosphomimetic variants and the WT protein at the same salt concentrations. The experimental and in silico data were also remarkably close at the quantitative level, with protein concentrations at the phase boundaries differing by only a few micromolar.

Our coarse-grained modeling-based analysis of forces acting on the proteins in a phase separated state did not support the possibility that attractive electrostatic intermolecular forces per se drive LLPS of the phosphomimetic variants in their low salt regimes. According to our simulations, total intermolecular hydrophobic forces eclipsed total intermolecular electrostatic forces by two orders of magnitude in both the low and high salt regimes for all TDP-43 LCD variants studied. These in silico data were further supported by the observation that condensates of the phosphomimetic variants that were formed in the absence of NaCl, and thus in the absence of any salt screening, were similarly highly sensitive to 1,6-hexanediol as condensates that were formed in the high salt regime (Kroschwald et al., 2015). Although the mechanism of how 1,6-hexanediol disrupts protein LLPS is not completely clear, it is a standard and widely used tool for disrupting hydrophobic interactions, which strongly suggests that, for all three TDP-43 LCD variants, droplet formation in the low salt regime heavily involved hydrophobic forces. In contrast, condensates of proteins whose LLPS is primarily electrostatically driven, such as tau and C9orf72 dipeptide repeats, exhibit a considerable resistance to 1,6-hexanediol (Boeynaems et al., 2017; Boyko et al., 2019).

Our cumulative data suggest that even though hydrophobic interactions are a major driver of the LLPS of 2-PM and 4-PM TDP-43 LCD variants, electrostatic forces play an important modulatory role in this process. This is due to the polarized charge distributions of these phosphomimetic protein variants, which leads to significant attractive intermolecular electrostatic interactions. We propose that these attractive electrostatic forces, which act over longer distances compared to hydrophobic forces at low salt concentrations (Israelachvili & Pashley, 1982), bring protein monomers together. This, in turn, promotes shorter-range hydrophobic interactions that are a major driving force for LLPS. Since (attractive) electrostatic forces decrease with an increase in ionic strength, there

is an inverse salt dependence of LLPS for phosphomimetic variants in the low salt regime. In contrast, electrostatic forces experienced by WT TDP-43 LCD at low salt concentrations are repulsive. Thus, in this latter case, NaCl promotes LLPS by simultaneously decreasing (repulsive) electrostatic interactions and promoting hydrophobic interactions at all salt concentrations.

The main purpose of our present study was to gain mechanistic understanding of the effect of pathologically relevant C-terminal phosphomimetic substitutions on TDP-43 LCD LLPS. To achieve this objective, it was necessary to explore LLPS over a broad range of NaCl concentrations. From a biological perspective, however, the LLPS behavior of these proteins at physiologic ionic strength is of special interest. Our data revealed that at 150 mM NaCl, WT TDP-43 LCD phase separates more robustly than the C-terminal phosphomimetic variants, even though this difference is rather modest (the c_{sat}'s of all three proteins fell within a 4 μM range). It should be noted, however, that authentic phosphorylation may impart larger negative charge than a phosphomimetic substitution; thus, the difference in LLPS propensity between unmodified and phosphorylated proteins would likely be substantially larger. Furthermore, LLPS of full-length TDP-43 inside the cell is likely further modified by the N-terminal protein domains as well as other biomolecules, such as RNA and other proteins, and bulky phosphate groups may engage in more stereospecific interactions with these partner domains/molecules as compared to phosphomimetic residues (Conicella et al., 2016; Haider et al., 2023; Wang et al., 2018). Nonetheless, our present findings for homotypic TDP-43 LCD LLPS obtained using a simple phosphomimetic model provide a physicochemical foundation for the interpretation of future studies on the effect of phosphorylation on TDP-43 LLPS in a complex cellular environment.

4 | MATERIALS AND METHODS

4.1 | Expression and purification of WT and C-terminally phosphomimetic TDP-43

We used site-directed mutagenesis on a plasmid encoding the amino acid sequence of WT TDP-43 LCD (residues 266–414) with an N-terminal His_6 tag and thrombin cleavage site (MRGSHHHHHHGMASLVPRGS) in a pRSET-B vector to make an analogous plasmid construct for S403D/S404D (2-PM) and S403D/S404D/S409D/S410D (4-PM) TDP-43 LCD. Rosetta *Escherichia coli* was used to express the proteins, and they were purified as previously described (Babinchak et al., 2019), except that thrombin protease (Cytiva Life Sciences, Marlborough, Massachusetts) was used to cleave the N-terminal tag after FPLC and before HPLC. The post-FPLC protein was diluted by a factor of 16 into a 20 mM potassium phosphate (pH 6) solution. Immediately following this step, thrombin was added (15 U thrombin:1 mg of uncleaved TDP-43 LCD), and the solution was rocked for 48 h at ambient temperature. The cleaved protein was then concentrated (4-fold), and subsequently mixed with guanidinium hydrochloride such that the final concentration of GuHCl was 5.3 M. The mixture was then rocked for 30 min until the solution clarified. Subsequently, the solution was concentrated, buffer-exchanged on HPLC, and lyophilized as previously described (Babinchak et al., 2019). To determine the concentrations of protein stocks, we employed absorbance at 280 nm using an extinction coefficient of 17,990 M^{-1} cm^{-1}.

4.2 | Turbidity measurements

Turbidity (absorbance at 600 nm) at 25°C was employed to measure the extent of phase separation, using a Tecan (Baldwin Park, California) Spark multimode microplate reader with Te-Cool active temperature control. Experiments were carried out in 20 mM potassium phosphate buffer (pH 7.4) containing NaCl at different concentrations.

4.3 | Fluorescence microscopy imaging

Sample was prepared in 20 mM potassium phosphate buffer (pH 7.4), at varying NaCl concentrations. Fluorescence microscopy was employed to visualize the sample, using Alexa Fluor 488-labeled protein, with a 1:20 ratio of labeled-to-unlabeled protein. 20 μl volumes of protein were plated on 35 mm dishes precoated with 1% Pluronic F-127 (Sigma Aldrich, St. Louis, Missouri). Subsequently, images were collected at ambient temperature on a Keyence (Itasca, Illinois) BZ-X710 microscope with a ×100/1.45 numerical aperture oil-immersion lens.

To prepare fluorescent probe, TDP-43 LCD was labeled with Alexa Fluor 488 NHS (succinimidyl) ester by adding 10 μl of dye in DMSO (10 mg/ml) to 100 μl of the protein (10 mg/ml) in a solution of 20 mM potassium phosphate (pH 7) buffer. The labeling reaction was conducted at ambient temperature, under quiescent conditions. After 1 h, the reaction was terminated by adding an equivalent volume of 20 mM potassium phosphate (pH 7) buffer with 4 M guanidinium hydrochloride; Zeba desalting columns (Thermo Fisher Scientific, Waltham, MA) were used to clear excess dye and buffer exchange

the final product into 20 mM potassium phosphate (pH 7) buffer with 4 M guanidinium hydrochloride.

4.4 | Phase diagrams and saturation concentrations

Phase separation diagrams were constructed based on turbidity measurements, with boundaries of phase separation defined as OD at 600 nm of ≥ 0.02 (which corresponds to the threshold OD that could be reproducibly determined in these experiments). LLPS in the boundary regions was confirmed by fluorescence microscopy. To determine the saturation concentration of a TDP-43 variant under a particular condition, OD was monitored as a function of protein concentration. The concentration at which two straight lines drawn through experimental data points intersected corresponded to c_{sat} (Boyko et al., 2020).

5 | COMPUTATIONAL METHODS

5.1 | Simulation framework: Coarse grained parametrization

To explore the relative importance of electrostatic and hydrophobic interactions in maintaining liquid–liquid phase separation (LLPS) of TDP-43 LCD, a coarse-grained simulation framework was developed. Though coarse-grained modeling does not capture the same level of detail as atomistic modeling, the substantially lower computational expense allowed for large enough timescales to observe phase separation. We implemented this framework using previously established methods (Dignon et al., 2018; Regy et al., 2021), where every amino acid was approximated as a soft sphere defined by four properties: mass (m), charge (q), hydrophobicity (λ), and size (σ) (Table S1) (Dignon et al., 2018). The Kapcha-Rossky Hydrophobicity scale (HPS-KR) was used for hydrophobicity values (Kapcha & Rossky, 2014).

To model amino acid bonds in the simulation framework, consecutive amino acids were approximated as being connected with a "spring" and bound together with a harmonic potential of the form:

$$\varphi_s(r) = \frac{1}{2}k(r - r_0)^2$$

where k was the "spring" constant between bound amino acids and r_0 was the bond rest length ($k = 8305\ \frac{\text{kJ}}{\text{mol nm}^2}$, $r_0 = 0.38$ nm for all simulations). Two types of pairwise interactions were accounted for in our simulations: electrostatic interactions and soft interactions. Electrostatic interactions were modeled using an electrostatic potential with Debye screening:

$$\varphi_E{}^{ij}(r) = \frac{q^i q^j}{4\pi\varepsilon_r\varepsilon_0 r} e^{\frac{-r}{\lambda_D}}$$

where q^i and q^j were the charges of the interacting particles, ε_r was the relative permittivity of the medium (water), ε_0 was the permittivity of free space, r was the distance between interacting particles and λ_D was the Debye screening length. All simulations were run in the presence of a buffer solution. Specifically, a 20 mM potassium phosphate buffer solution composed of 70% dibasic potassium phosphate and 30% monobasic potassium phosphate. The buffer solution was modeled in simulations by including the ions present therein as a contribution to the Debye screening length (λ_D was between 1.64 and 0.267 nm for tested salt concentrations). Electrostatic interactions were calculated only for particle pairs within 3.5 nm for computational efficiency. To capture soft interactions, the Ashbaugh–Hatch functional form (Ashbaugh & Hatch, 2008) was used to generate a modified Lennard–Jones potential (MLJ):

$$\varphi^{ij}{}_{MLJ}(r) = \begin{cases} 4\varepsilon\left[\left(\frac{\sigma^{ij}}{r}\right)^{12} - \left(\frac{\sigma^{ij}}{r}\right)^{6}\right] + \varepsilon\left(1 - \lambda^{ij}\right) \text{ If } r \le 2^{\frac{1}{6}}\sigma^{ij} \\ \lambda^{ij} 4\varepsilon\left[\left(\frac{\sigma^{ij}}{r}\right)^{12} - \left(\frac{\sigma^{ij}}{r}\right)^{6}\right] \text{ If } r > 2^{\frac{1}{6}}\sigma^{ij} \end{cases}$$

where ε was the depth of the potential well ($\varepsilon = 0.1985$–$0.205\ \frac{\text{kcal}}{\text{mol}}$ for tested salt concentrations), σ^{ij} was the average "size" of two interacting particles, λ^{ij} was the average hydrophobicity of two interacting particles and r was the distance between interacting particles. The term:

$$4\varepsilon\left[\left(\frac{\sigma^{ij}}{r}\right)^{12} - \left(\frac{\sigma^{ij}}{r}\right)^{6}\right]$$

is the typical 12–6 Lennard-Jones potential. We note that the hydrophobicity parameter λ^{ij} was present only in the attractive term of the MLJ interactions. Thus, when analyzing forces between amino acids, we defined attractive MLJ interactions as hydrophobic interactions. Simulations were run in the presence of NaCl, a weakly kosmotropic ion, meaning it stabilizes hydrophobic interresidue interactions. In terms of our model, this was implemented by increasing either the well depth (ε), or the hydrophobicity parameter (λ^{ij}) of the MLJ potential. Wohl et al. (2021) have explored methods by which to

adjust the hydrophobicity parameter, while we took the approach of adjusting the well-depth. Both of these methods produce qualitatively similar results (Figure S2 and Table S2), discussed in more detail below. We made the well depth of the MLJ potential explicitly salt-dependent with a simple first order perturbation:

$$\varepsilon \rightarrow \varepsilon(c_{\mathrm{NaCl}}) = \varepsilon_{\mathrm{b}} + \alpha c_{\mathrm{NaCl}}$$

where α ($0.0052\ \frac{\mathrm{kcal}}{\mathrm{mol}}\mathrm{M}^{-1}$) was the rate of change of well depth with respect to NaCl concentration, and ε_{b} ($0.1985\ \frac{\mathrm{kcal}}{\mathrm{mol}}$) was the baseline well depth. MLJ interactions were calculated only for particle pairs within 2 nm for computational efficiency.

5.2 | Simulation framework: workflow

Simulations of TDP-43 LCD and its phosphomimetic variants were performed using the Python toolkit HooMD-Blue (Anderson et al., 2020; Howard et al., 2018). For our simulations, the number of proteins in the box was intentionally kept small ($N \leq 54$) to allow for many regions of the protein/salt concentration parameter space to be explored. For all main text simulations, the simulation box was initially squeezed to a size of 60 nm^3. Then, the simulation box was extended to a slab configuration (60 nm × 60 nm × 1200 nm) with periodic boundary conditions (Blas et al., 2008; Dignon et al., 2018; Silmore et al., 2017). This setup allowed us to roughly mimic a larger system, though some finite size effects remained. To test the significance of finite size effects, we also ran simulations with larger numbers of proteins in a larger box (see details below). In all cases, simulations were run for 5 μs in 0.01 ps time steps propagated in time using Langevin dynamics. The system equilibrated during the first 4 μs of the simulation, and the system was analyzed during the final 1 μs.

5.3 | Phase separation validation

As a proof of concept of the efficacy of the outlined simulation framework, phase separation diagrams over a range of salt concentrations (0–1250 mM) and protein concentrations (9.6–20.8 μM) were generated and compared to experimental results. The MLJ well depth and its rate of change with respect to NaCl concentration were tuned such that simulated and experimental phase separation diagrams corresponded to both 0 and 1250 mM NaCl for TDP-43-LCD. Thus, the experimental phase separation diagrams at 0 and 1250 mM salt concentration constituted boundary conditions to which the explicit salt dependence of the MLJ well depth was matched.

For each data point in the salt/protein concentration space, a simulation was run and a binary classification of "phase separated" or "dissolved" was made. This classification was rendered after visualizing the simulation results over the entire 5 μs period. Proteins with center of masses within 10 nm were classified as in the same cluster. If the number of neighbors (proteins in the same cluster) per protein was >2 for the entirety of the last microsecond, the datapoint was classified as "phase separated." Otherwise, the datapoint was classified as "dissolved." For a given NaCl concentration, all protein concentrations greater than the lowest protein concentration at which "phase separation" was observed were assumed to be "phase separated" as well. Conversely, all protein concentrations less than the lowest protein concentration at which "phase separation" was observed were assumed to be "dissolved." Duplicates of the phase separation diagram ($N = 2$) were generated, and the final combined simulation phase diagrams are displayed in Figure 2c. They clearly recapitulated the important qualitative features of the experimental diagrams. In the final combined phase separation diagrams, points classified as phase separated had to be verified by both simulations. Different numerical seeds were used for each duplicate simulation. The different seeds generated a different array of randomized thermal fluctuations, ensuring that results between the two duplicates were uncorrelated.

To stress the importance of an explicitly salt-dependent MLJ well depth, the WT TDP-43 LCD and 4-PM phosphomimetic variant phase separation diagrams were generated with simulations run at a constant MLJ well depth ($\varepsilon = 0.205\ \frac{\mathrm{kcal}}{\mathrm{mol}}$). These results can be seen in (Figure S1), and of note, do not recapitulate the experimental phase separation diagrams as well as the salt-dependent MLJ well depth phase diagrams do.

We accounted for NaCl-dependent hydrophobic interactions by increasing the well depth (ε) of the MLJ according to a simple first order perturbation; another study used an alternative approach in which they accounted for NaCl-dependent hydrophobic interactions by instead adjusting the hydrophobicity parameters (λ) (Wohl et al., 2021). To show that our approach is qualitatively similar to the latter, we generated the WT and 4-PM phase separation diagrams according to the λ adjustment model (Wohl et al., 2021). These results can be seen in (Figure S2), and of note, produce qualitatively similar results to the diagrams generated using our first order adjustment to the well depth. To further investigate the similarities between the two methods, we rank ordered the hydrophobicity values in three cases: the original values, the values after adjustment according to

the λ adjustment model at 0 mM NaCl and the values after adjustment according to the λ adjustment model at 1250 mM NaCl. Notably, in all three cases, the rank ordering of the hydrophobicities were almost identical, indicating that we can model qualitatively similar interactions between proteins using either the adjustment to ε or λ (Table S2).

To validate that our approach of using a relatively small number of proteins ($N \leq 54$) did not suffer from significant finite size effects, a subset of the phase separation diagrams was generated with protein counts between 125 and 270 for comparison. For these simulations, the simulation box was initially squeezed to a size of (60 nm × 60 nm × 300 nm), and the resulting slab was (60 nm × 60 nm × 5800 nm).

With the larger protein counts, the MLJ well depth ($\varepsilon_b = 0.1875 \frac{\text{kcal}}{\text{mol}}$) and its rate of change with respect to NaCl concentration ($\alpha = 0.0024 \frac{\text{kcal}}{\text{mol}} \text{M}^{-1}$) were recalibrated at 0 and 1250 mM NaCl in the same manner described previously in these methods ($\varepsilon = 0.1875$–$0.1905 \frac{\text{kcal}}{\text{mol}}$ for tested salt concentrations). With these new well depth values and larger protein counts, the 0, 200 and 1250 mM NaCl concentration phase separation diagram columns were regenerated for TDP-43-LCD and the 4-PM phosphomimetic variant. These results can be seen in (Figure S5), and of note, largely recapitulate the data produced by the smaller protein count simulations.

5.4 | Electrostatic and hydrophobic force analyses

With the efficacy of the simulation framework validated, we then aimed to quantify the relative importance of electrostatic and hydrophobic interactions in maintaining LLPS over a range of salt concentrations. A natural quantity to use for this purpose was the forces generated by electrostatic interactions and hydrophobic interactions. We performed this analysis at a protein concentration of 20.8 μM, as at this protein concentration all of the TDP-43 LCD variants phase separated at every NaCl concentration tested in silico.

From 0 to 1000 mM NaCl, the time-averaged electrostatic and time-averaged hydrophobic forces were calculated between each pair of amino acids in the simulation box over the final microsecond of each simulation. Using the time-averaged forces, two quantities were calculated: (i) the sum of the time-averaged electrostatic forces and (ii) the sum of the time-averaged hydrophobic forces. These results were plotted against salt concentration (Figures 3a and 4a). Error bars for these data points represent one standard deviation, and were generated using a block bootstrapping procedure with 50 blocks and 1000 resamples.

After establishing the relative importance of hydrophobic forces to electrostatic forces, we analyzed which regions of proteins were interacting most strongly in the phase separated state. To accomplish this end, the sum of the time-averaged intermolecular electrostatic forces and the sum of the time-averaged intermolecular hydrophobic forces were calculated for each amino acid residue in a pairwise association with every other amino acid residue in every protein in the box. A heat map was generated showing these sums for all residue-residue interactions (Figures 5, 6 and S3).

5.5 | Code availability

All code used for this project is available at the following Github repository: https://github.com/hincz-lab/TDP_43_Phase_Separation.

AUTHOR CONTRIBUTIONS

Raza Haider: Conceptualization; data curation; formal analysis; funding acquisition; investigation; methodology; validation; visualization; writing – original draft; writing – review and editing. **Brandon Shipley:** Data curation; formal analysis; investigation; methodology; software; validation; visualization; writing – review and editing. **Krystyna Surewicz:** Resources. **Michael Hinczewski:** Formal analysis; funding acquisition; methodology; project administration; resources; supervision; writing – review and editing. **Witold K. Surewicz:** Conceptualization; formal analysis; funding acquisition; methodology; project administration; resources; supervision; writing – review and editing.

FUNDING INFORMATION

This study was supported in part by National Institutes of Health Grants RF1 AG061797 (to Witold K. Surewicz), F30 AG071339-03 (to Raza Haider), T32 NS077888, and T32 GM007250. The content is solely the responsibility of the authors and does not necessarily represent the official views of the National Institutes of Health.

CONFLICT OF INTEREST STATEMENT

The authors declare no conflict of interest.

ORCID

Witold K. Surewicz https://orcid.org/0000-0001-7940-6027

REFERENCES

Alberti S, Dormann D. Liquid-Liquid Phase Separation in Disease. Annu Rev Genet. 2019;53:171–94.

Anderson J, Glaser J, Glotzer SC. HOOMD-blue: a python package for high-performance molecular dynamics and hard particle Monte Carlo simulations. Comput Mater Sci. 2020;173:109363.

Arai T, Hasegawa M, Akiyama H, Ikeda K, Nonaka T, Mori H, et al. TDP-43 is a component of ubiquitin-positive tau-negative inclusions in frontotemporal lobar degeneration and amyotrophic lateral sclerosis. Biochem Biophys Res Commun. 2006; 351(3):602–11.

Arseni D, Hasegawa M, Murzin AG, Kametani F, Arai M, Yoshida M, et al. Structure of pathological TDP-43 filaments from ALS with FTLD. Nature. 2022;601(7891):139–43.

Ashbaugh HS, Hatch HW. Natively unfolded protein stability as a coil-to-globule transition in charge/hydropathy space. J Am Chem Soc. 2008;130(29):9536–42.

Babinchak WM, Dumm BK, Venus S, Boyko S, Putnam AA, Jankowsky E, et al. Small molecules as potent biphasic modulators of protein liquid-liquid phase separation. Nat Commun. 2020;11(1):5574.

Babinchak WM, Haider R, Dumm BK, Sarkar P, Surewicz K, Choi JK, et al. The role of liquid-liquid phase separation in aggregation of the TDP-43 low-complexity domain. J Biol Chem. 2019;294(16):6306–17.

Babinchak WM, Surewicz WK. Liquid-liquid phase separation and its mechanistic role in pathological protein aggregation. J Mol Biol. 2020;432(7):1910–25.

Banani SF, Lee HO, Hyman AA, Rosen MK. Biomolecular condensates: organizers of cellular biochemistry. Nat Rev Mol Cell Biol. 2017;18(5):285–98.

Blas FJ, MacDowell LG, de Miguel E, Jackson G. Vapor-liquid interfacial properties of fully flexible Lennard-Jones chains. J Chem Phys. 2008;129(14):144703.

Boeynaems S, Bogaert E, Kovacs D, Konijnenberg A, Timmerman E, Volkov A, et al. Phase separation of C9orf72 dipeptide repeats perturbs stress granule dynamics. Mol Cell. 2017;65(6):1044–1055 e5.

Boyko S, Qi X, Chen TH, Surewicz K, Surewicz WK. Liquid-liquid phase separation of tau protein: the crucial role of electrostatic interactions. J Biol Chem. 2019;294(29):11054–9.

Boyko S, Surewicz K, Surewicz WK. Regulatory mechanisms of tau protein fibrillation under the conditions of liquid-liquid phase separation. Proc Natl Acad Sci USA. 2020;117(50):31882–90.

Buratti E. Functional significance of TDP-43 mutations in disease. Adv Genet. 2015;91:1–53.

Carey JL, Guo L. Liquid-liquid phase separation of TDP-43 and FUS in physiology and pathology of neurodegenerative diseases. Front Mol Biosci. 2022;9:826719.

Conicella AE, Dignon GL, Zerze GH, Schmidt HB, D'Ordine AM, Kim YC, et al. TDP-43 alpha-helical structure tunes liquid-liquid phase separation and function. Proc Natl Acad Sci USA. 2020;117(11):5883–94.

Conicella AE, Zerze GH, Mittal J, Fawzi NL. ALS mutations disrupt phase separation mediated by alpha-helical structure in the TDP-43 low-complexity C-terminal domain. Structure. 2016; 24(9):1537–49.

de Boer EMJ, Orie VK, Williams T, Baker MR, de Oliveira HM, Polvikoski T, et al. TDP-43 proteinopathies: a new wave of neurodegenerative diseases. J Neurol Neurosurg Psychiatry. 2020;92(1):86–95.

Dignon GL, Zheng W, Kim YC, Best RB, Mittal J. Sequence determinants of protein phase behavior from a coarse-grained model. PLoS Comput Biol. 2018;14(1):e1005941.

Eck RJ, Kraemer BC, Liachko NF. Regulation of TDP-43 phosphorylation in aging and disease. Geroscience. 2021;43(4):1605–14.

François-Moutal L, Perez-Miller S, Scott DD, Miranda VG, Mollasalehi N, Khanna M. Structural insights into TDP-43 and effects of post-translational modifications. Front Mol Neurosci. 2019;12:301.

Furukawa Y, Kaneko K, Watanabe S, Yamanaka K, Nukina N. A seeding reaction recapitulates intracellular formation of Sarkosyl-insoluble transactivation response element (TAR) DNA-binding protein-43 inclusions. J Biol Chem. 2011;286(21): 18664–72.

Gruijs da Silva LA, Simonetti F, Hutten S, Riemenschneider H, Sternburg EL, Pietrek LM, et al. Disease-linked TDP-43 hyperphosphorylation suppresses TDP-43 condensation and aggregation. EMBO J. 2022;41(8):e108443.

Haider R, Boyko S, Surewicz WK. Liquid–liquid phase separation in neurodegenerative diseases. In: Uversky V, editor. Droplets of life. Cambridge, MA: Academic Press; 2023. p. 619–50.

Haider R, Penumutchu S, Boyko S, Surewicz WK. Phosphomimetic substitutions in TDP-43's transiently alpha-helical region suppress phase separation. Biophys J. 2024;123:361–73.

Hasegawa M, Arai T, Nonaka T, Kametani F, Yoshida M, Hashizume Y, et al. Phosphorylated TDP-43 in frontotemporal lobar degeneration and amyotrophic lateral sclerosis. Ann Neurol. 2008;64(1):60–70.

Howard MP, Panagiotopoulos AZ, Nikoubashman A. Efficient mesoscale hydrodynamics: multiparticle collision dynamics with massively parallel GPU acceleration. Comput Phys Commun. 2018;230:10–20.

Igaz LM, Kwong LK, Xu Y, Truax AC, Uryu K, Neumann M, et al. Enrichment of C-terminal fragments in TAR DNA-binding protein-43 cytoplasmic inclusions in brain but not in spinal cord of frontotemporal lobar degeneration and amyotrophic lateral sclerosis. Am J Pathol. 2008;173(1):182–94.

Israelachvili J, Pashley R. The hydrophobic interaction is long range, decaying exponentially with distance. Nature. 1982; 300(5890):341–2.

Jiang LL, Che MX, Zhao J, Zhou CJ, Xie MY, Li HY, et al. Structural transformation of the amyloidogenic core region of TDP-43 protein initiates its aggregation and cytoplasmic inclusion. J Biol Chem. 2013;288(27):19614–24.

Johnson BS, Snead D, Lee JJ, McCaffery JM, Shorter J, Gitler AD. TDP-43 is intrinsically aggregation-prone, and amyotrophic lateral sclerosis-linked mutations accelerate aggregation and increase toxicity. J Biol Chem. 2009;284(30):20329–39.

Joseph JA, Espinosa JR, Sanchez-Burgos I, Garaizar A, Frenkel D, Collepardo-Guevara R. Thermodynamics and kinetics of phase separation of protein-RNA mixtures by a minimal model. Biophys J. 2021;120:1219–30.

Kapcha LH, Rossky PJ. A simple atomic-level hydrophobicity scale reveals protein interfacial structure. J Mol Biol. 2014;426(2): 484–98.

Krainer G, Welsh TJ, Joseph JA, Espinosa JR, Wittmann S, de Csilléry E, et al. Reentrant liquid condensate phase of proteins

is stabilized by hydrophobic and non-ionic interactions. Nat Commun. 2021;12(1):1085.

Kroschwald S, Maharana S, Mateju D, Malinovska L, Nüske E, Poser I, et al. Promiscuous interactions and protein disaggregases determine the material state of stress-inducible RNP granules. Elife. 2015;4:e06807.

Li HR, Chen TC, Hsiao CL, Shi L, Chou CY, Huang JR. The physical forces mediating self-association and phase-separation in the C-terminal domain of TDP-43. Biochim Biophys Acta Proteins Proteom. 2018;1866(2):214–23.

Li HR, Chiang WC, Chou PC, Wang WJ, Huang JR. TAR DNA-binding protein 43 (TDP-43) liquid-liquid phase separation is mediated by just a few aromatic residues. J Biol Chem. 2018; 293(16):6090–8.

Martin EW, Thomasen FE, Milkovic NM, Cuneo MJ, Grace CR, Nourse A, et al. Interplay of folded domains and the disordered low-complexity domain in mediating hnRNPA1 phase separation. Nucleic Acids Res. 2021;49(5):2931–45.

Meneses A, Koga S, O'Leary J, Dickson DW, Bu G, Zhao N. TDP-43 pathology in Alzheimer's disease. Mol Neurodegener. 2021;16(1):84.

Moelbert S, Normand B, De Los Rios P. Kosmotropes and chaotropes: modelling preferential exclusion, binding and aggregate stability. Biophys Chem. 2004;112(1):45–57.

Mohanty P, Shenoy J, Rizuan A, Mercado-Ortiz JF, Fawzi NL, Mittal J. A synergy between site-specific and transient interactions drives the phase separation of a disordered, low-complexity domain. Proc Natl Acad Sci U S A. 2023;120(34):e2305625120.

Monahan Z, Ryan VH, Janke AM, Burke KA, Rhoads SN, Zerze GH, et al. Phosphorylation of the FUS low-complexity domain disrupts phase separation, aggregation, and toxicity. EMBO J. 2017;36(20):2951–67.

Murthy AC, Dignon GL, Kan Y, Zerze GH, Parekh SH, Mittal J, et al. Molecular interactions underlying liquid-liquid phase separation of the FUS low-complexity domain. Nat Struct Mol Biol. 2019;26(7):637–48.

Neumann M, Frick P, Paron F, Kosten J, Buratti E, Mackenzie IR. Correction to: antibody against TDP-43 phosphorylated at serine 369 suggests conformational differences of TDP-43 aggregates among FTLD-TDP subtypes. Acta Neuropathol. 2021;141(1):137.

Neumann M, Kwong LK, Lee EB, Kremmer E, Flatley A, Xu Y, et al. Phosphorylation of S409/410 of TDP-43 is a consistent feature in all sporadic and familial forms of TDP-43 proteinopathies. Acta Neuropathol. 2009;117(2):137–49.

Neumann M, Sampathu DM, Kwong LK, Truax AC, Micsenyi MC, Chou TT, et al. Ubiquitinated TDP-43 in frontotemporal lobar degeneration and amyotrophic lateral sclerosis. Science. 2006; 314(5796):130–3.

Nonaka T, Kametani F, Arai T, Akiyama H, Hasegawa M. Truncation and pathogenic mutations facilitate the formation of intracellular aggregates of TDP-43. Hum Mol Genet. 2009;18(18):3353–64.

Prasad A, Bharathi V, Sivalingam V, Girdhar A, Patel BK. Molecular mechanisms of TDP-43 misfolding and pathology in amyotrophic lateral sclerosis. Front Mol Neurosci. 2019;12:25.

Regy RM, Zheng W, Mittal J. Using a sequence-specific coarse-grained model for studying protein liquid-liquid phase separation. Methods Enzymol. 2021;646:1–17.

Ryan VH, Dignon GL, Zerze GH, Chabata CV, Silva R, Conicella AE, et al. Mechanistic view of hnRNPA2 low-complexity domain structure, interactions, and phase separation altered by mutation and arginine methylation. Mol Cell. 2018;69(3):465–479 e7.

Schmidt HB, Barreau A, Rohatgi R. Phase separation-deficient TDP43 remains functional in splicing. Nat Commun. 2019; 10(1):4890.

Schmidt HB, Rohatgi R. In vivo formation of vacuolated multi-phase compartments lacking membranes. Cell Rep. 2016;16(5): 1228–36.

Shin Y, Brangwynne CP. Liquid phase condensation in cell physiology and disease. Science. 2017;357(6357):eaaf4382.

Silmore KS, Howard MP, Panagiotopoulos AZ. Vapour–liquid phase equilibrium and surface tension of fully flexible Lennard–Jones chains. Mol Phys. 2017;115(3):320–7.

Wang A, Conicella AE, Schmidt HB, Martin EW, Rhoads SN, Reeb AN, et al. A single N-terminal phosphomimic disrupts TDP-43 polymerization, phase separation, and RNA splicing. EMBO J. 2018;37(5):e97452.

Wang B, Zhang L, Dai T, Qin Z, Lu H, Zhang L, et al. Liquid-liquid phase separation in human health and diseases. Signal Transduct Target Ther. 2021;6(1):290.

Wohl S, Jakubowski M, Zheng W. Salt-dependent conformational changes of intrinsically disordered proteins. J Phys Chem Lett. 2021;12(28):6684–91.

Yang C, Tan W, Whittle C, Qiu L, Cao L, Akbarian S, et al. The C-terminal TDP-43 fragments have a high aggregation propensity and harm neurons by a dominant-negative mechanism. PLoS One. 2010;5(12):e15878.

Zbinden A, Pérez-Berlanga M, de Rossi P, Polymenidou M. Phase separation and neurodegenerative diseases: a disturbance in the force. Dev Cell. 2020;55(1):45–68.

SUPPORTING INFORMATION

Additional supporting information can be found online in the Supporting Information section at the end of this article.

How to cite this article: Haider R, Shipley B, Surewicz K, Hinczewski M, Surewicz WK. Pathological C-terminal phosphomimetic substitutions alter the mechanism of liquid–liquid phase separation of TDP-43 low complexity domain. Protein Science. 2024;33(10):e5179. https://doi.org/10.1002/pro.5179